Ordering mechanisms in two-dimensional sphere-forming block copolymers

Daniel A. Vega
Department of Physics, Universidad Nacional del Sur, B8000CPB Bahía Blanca, Argentina

Christopher K. Harrison and Dan E. Angelescu
Schlumberger-Doll Research Center, 36 Old Quarry Road, Ridgefield, Connecticut 06877, USA

Matthew L. Trawick,* David A. Huse, and Paul M. Chaikin
Department of Physics, Princeton University, Princeton, New Jersey 08544, USA

Richard A. Register
Department of Chemical Engineering, Princeton University, Princeton, New Jersey 08544, USA
(Received 30 January 2005; published 29 June 2005)

We study the coarsening dynamics of two-dimensional hexagonal patterns formed by single microdomain layers of block copolymers, using numerical simulations. Our study is focused on the temporal evolution of the orientational correlation length, the interactions between topological defects, and the mechanisms of coarsening. We find no free disclinations in the system; rather, they are located on large-angle grain boundaries, commonly where such boundaries bifurcate. The correlation lengths determined from the scattering function, from the density of dislocations, and from the density of disclinations exhibit similar behavior and grow with time according to a power law. The orientational correlation length also grows following a power law, but with a higher exponent than the other correlation lengths. The orientational correlation length grows via annihilation of dislocations, through preferential annihilation of small-angle grain boundaries due to poor screening of the strain field around dislocations located on small-angle grain boundaries. Consequently, the patterns are characterized by large-angle grain boundaries. The most commonly observed mechanism of coarsening is the collapse of smaller grains residing on the boundary of two larger grains delimited by large-angle grain boundaries. Simulations agree remarkably well with experimental results recently obtained.

DOI: 10.1103/PhysRevE.71.061803 PACS number(s): 36.20.−r, 81.10.−h

I. INTRODUCTION

As a consequence of their ability to self-assemble into nanoscale ordered structures block copolymers have received great attention in recent years. In particular, in diblock copolymers the existence of four equilibrium structures has been experimentally confirmed [1]: lamellae, hexagonally ordered cylinders, bicontinuous cubic gyroids, and spheres packed on a body-centered cubic lattice. Theoretical modeling with a self-consistent field theory has successfully described the existence of these phases as equilibrium structures [2,3].

The ability of block copolymers to self-assemble into nanoscale structures has been recently used to obtain quantum dot arrays for lasers [4] and high-density arrays of magnetic domains for information storage [5–7]. However, the use of block copolymers to obtain lithographic masks for electronic applications requires the production of long-range order and good control over the density of defects [8,9]. For example, it is well known that dislocations destroy the translational order, while disclinations dramatically reduce both translational and orientational order. In addition, other defects such as undulations, grain boundaries, or Eckhaus instabilities also affect the order of the pattern. To get good control over the ordering process, it is important to determine the mechanisms that dominate its evolution towards thermodynamic equilibrium.

Recently, by using an atomic force microscope in tapping mode, taking advantage of the difference in modulus between the two blocks of a polystyrene-poly(ethylene-*alt*-propylene) block copolymer, Harrison *et al.* have tracked the time evolution of the density of defects and the orientational correlation length of cylinder-forming [8,9] and sphere-forming [10,11] block copolymer thin films. By tracking the density of disclinations it was found that the dominant mechanism of coarsening in cylinder-forming block copolymers (striped patterns) involves the annihilation of three or four disclinations ("multipoles") and that the orientational correlation length $\xi_2(t)$ grows with time according to a power law with an exponent of $1/4$ [$\xi_2(t) \sim t^{1/4}$] [8,9]. In the sphere-forming system it was experimentally found that the orientational correlation length also scales with time with an exponent of $1/4$ [$\xi_6(t) \sim t^{1/4}$], although the mechanism of coarsening was different. In this case, it was observed that most of the dislocations and disclinations condense into grain boundaries and the coarsening process is dominated by the annihilation of smaller grains residing on the boundary of two larger grains. In addition, characteristic correlation lengths obtained from the densities of dislocations and disclinations also grew following a power law, but with a slightly smaller exponent ($\sim 1/5$) [11].

*Present address: Department of Physics, University of Richmond, Richmond, VA 23173, USA.

Although with the atomic force microscopy (AFM) technique it is possible to accurately track the orientational correlation length, in the sphere-forming system it is difficult to follow the motion of individual defects. Although time resolution can be controlled by adjusting the annealing temperature, experimental difficulties such as piezoelectric creep in the AFM [12] make the accurate determination of the motion of individual dislocations and disclinations very difficult. On the other hand, computer simulations have been used extensively to predict the evolution towards equilibrium structures [13,14], shear induced instabilities [15], interface dynamics [16], and the effect of directional quenching [17]. Most of these studies, however, have been focused on the lamellar phase. To the best of our knowledge, there have been no studies concerning the relationship between correlation lengths and topological defects in structures other than lamellae. In addition, at present there is no comparison between recent experimental data and simulation results.

In this work we study the kinetics of coarsening of a two-dimensional block copolymer hexagonal phase, with the cell dynamics method [18]. The dynamics are modeled following the standard time-dependent Ginzburg-Landau equation for a conserved order parameter and the mean field free energy functional for a diblock copolymer proposed by Ohta and Kawasaki [19,20]. The degree of ordering is studied by determining the scattering function, the orientational correlation length, and the densities of topological defects (dislocations and disclinations).

II. MODEL AND CELL DYNAMICS METHOD

The dynamics of microphase separation for a diblock copolymer in the absence of macroscopic flow can be described by the following time-dependent Ginzburg-Landau equation for a conserved order parameter (Cahn-Hillard-Cook equation) [13]:

$$\frac{\partial \psi}{\partial t} = M\nabla^2\left(\frac{\partial F}{\partial \psi}\right) + \zeta(\vec{r},t) \tag{1}$$

where the order parameter ψ is defined in terms of the local densities of each block in the block copolymer, M is a phenomenological mobility coefficient, $F(\psi)$ is the free energy functional for a diblock copolymer, and $\zeta(\vec{r},t)$ is a random noise term, with zero average and a second moment related to the mobility coefficient through the fluctuation-dissipation relation:

$$\langle \zeta(\vec{r},t)\zeta(\vec{r}',t')\rangle = -\eta M\nabla^2\delta(\vec{r}-\vec{r}')\delta(t-t'). \tag{2}$$

Here η is the noise strength, proportional to the temperature in the system after a quench below the order-disorder temperature. The free energy functional $F(\psi)$ includes a short-range and a long-range term, expressed as

$$F(\psi) = F_S(\psi) + F_L(\psi). \tag{3}$$

The short-range term has the form of a Landau free energy,

$$F_S(\psi) = \int d\vec{r}\left[H(\psi) + \frac{D}{2}(\vec{\nabla}\psi)^2\right] \tag{4}$$

where $H(\psi)$ represents the mixing free energy of the homogeneous blend of disconnected A and B homopolymers, the term containing the gradient represents the free energy penalty generated by the spatial variations of ψ (interfacial energy), and D is a diffusion coefficient. The free energy $H(\psi)$ in the functional given by Eq. (4) has the form

$$\mathrm{H}(\psi) = \tfrac{1}{2}[-\tau + \alpha(1-2f)^2]\psi^2 + \tfrac{1}{3}\lambda\psi^3 + \tfrac{1}{4}\mu\psi^4 \tag{5}$$

where α, λ, and μ are phenomenological constants and τ is a parameter related to the Flory-Huggins parameter χ through [17]

$$\tau = 8f(1-f)\rho_0\chi - \frac{2s(f)}{f(1-f)N}. \tag{6}$$

Here ρ_0 is the monomer density, $f=N_A/(N_A+N_B)$ is the A block fraction, $N=N_A+N_B$ is the total length of the diblock copolymer chain, where N_A and N_B are the chain lengths corresponding to each block, and for a given f, $s(f)$ is a constant of order unity. The long-range free energy contribution arises from the chain connectivity of the two blocks and can be expressed as [13,14]

$$F_L(\psi) = \frac{\beta}{2}\int d\vec{r}'\,d\vec{r}\,G(\vec{r}-\vec{r}')\psi(\vec{r})\psi(\vec{r}') \tag{7}$$

where $G(\vec{r}-\vec{r}')$ is the solution of $\nabla^2 G(\vec{r}) = -\delta(\vec{r})$ [14]. Although the parameters α, λ, μ, and β in the free energy expression can be derived from the vertex function given by Leibler [21], here we consider these parameters as phenomenological constants, chosen to obtain the desired phase.

In this work, Eq. (1) is simulated by the cell dynamics method on a two-dimensional square lattice. The evolution of the order parameter ψ can be expressed as [14,20]

$$\psi(\vec{n},t+1) = \Gamma(\psi(\vec{n},t)) - \langle\langle\Gamma(\psi(\vec{n},t)) - \psi(\vec{n},t)\rangle\rangle - \beta\psi(\vec{n},t) + \eta\tilde{\zeta}(\vec{n},t) \tag{8}$$

where

$$\Gamma(\psi(\vec{n},t)) = f(\psi(\vec{n},t)) + D[\langle\langle\psi(\vec{n},t)\rangle\rangle - \psi(\vec{n},t)] \tag{9}$$

and the map function $f(\psi(\vec{n},t))$ is given by [13,14]

$$f(\psi) = [1+\tau-\alpha(1-2f)^2]\psi - \lambda\psi^3 - \mu\psi^4. \tag{10}$$

Here $\vec{n}=(n_x,n_y)$ designates the lattice points and $\langle\langle\Xi\rangle\rangle$ represents an average over all neighbors of an arbitrary function Ξ, and is related to the isotropic Laplacian through [13]

$$\nabla^2\Xi = 3[\langle\langle\Xi\rangle\rangle - \Xi]. \tag{11}$$

For a two-dimensional system,

$$\langle\langle\Xi(\vec{r})\rangle\rangle = \frac{1}{6}\sum_{\vec{s}\in \mathrm{NN}}\Xi(\vec{s}) + \frac{1}{12}\sum_{\vec{s}\in \mathrm{NNN}}\Xi(\vec{s}) \tag{12}$$

where NN and NNN represent the nearest-neighbor and next-nearest-neighbor lattice sites, respectively [18]. It can be shown that by properly choosing the map function $f(\psi(\vec{n},t))$,

Eq. (8) corresponds to a particular discretization of Eq. (1). The term $\eta\tilde{\zeta}(\vec{n},t)$ in Eq. (8) represents a thermal noise (or external field). In this work the thermal noise is given by

$$\eta[\tilde{\zeta}_x(n_x+1,n_y,t)-\tilde{\zeta}_x(n_x,n_y,t)+\tilde{\zeta}_y(n_x,n_y+1,t)-\tilde{\zeta}_y(n_x,n_y,t)] \tag{13}$$

where η is the noise amplitude and $\tilde{\zeta}_x(n_x,n_y,t)$ and $\tilde{\zeta}_y(n_x,n_y,t)$ are random numbers uniformly distributed in the interval $[-1,1]$ [22,23]. Following this criterion, the random noise is a globally conserved quantity.

In our simulations the block copolymer composition was fixed at $f=0.25$, and the map function parameters, long-range strength, and diffusion coefficient were selected to be $\alpha=0.06$, $\tau=0.3$, $\mu=0.38$, $\lambda=0.23$, $\beta=0.03$, and $D=0.3$, respectively. The two-dimensional mean-field equilibrium structure for these parameters is hexagonal. The noise amplitude was fixed at $\eta=0.25$, except where indicated otherwise. This particular choice of noise amplitude yields results which are in very good agreement with the experiments. We have observed that in the absence of noise the pattern is frozen after a few simulation steps. Yokojima and Shiwa have also observed this feature in a similar system [24]. On the other hand, at large noise amplitudes ($n\approx 0.5$) the system undergoes an order-disorder transition induced by noise [25].

Our simulations employed cyclic boundary conditions, typically on a 512×512 lattice. However, a perfect hexagonal pattern can only match cyclic boundary conditions in the special case where the box and the pattern are commensurate; in all other cases, the imposition of cyclic boundary conditions introduces defects. To ensure that the few defects imparted by the boundary conditions did not dominate the results, some simulations were rerun on lattices with different dimensions, and were found to yield consistent results. The initial state was prepared by setting the order parameter to a uniformly random distribution in the interval $[-0.01,0.01]$.

III. ORDERING DYNAMICS

To evaluate the degree of ordering in the system we computed the circularly averaged scattering function $S(k,t)$ and the orientational correlation function $g_6(r,t)$. The scattering function is defined as

$$S(k,t)=\langle\tilde{\psi}(\vec{k},t)\tilde{\psi}^*(\vec{k},t)\rangle \tag{14}$$

where $\tilde{\psi}(\vec{k},t)$ represents the Fourier transform of the order parameter and $\vec{k}$ is the wave vector. Figure 1 shows simulation results for $kS(k,t)$ at two different stages of the coarsening process, corresponding to the patterns in Fig. 2. One immediately notices the increase in order in Fig. 2(b) as compared with Fig. 2(a). At short times it is possible to observe in Fig. 1 a liquidlike order, with a main peak characterizing the average distance between spheres. At long times, the scattering function shows an increase in the main peak intensity, a reduction in the peak width, and well-defined second-, third-, and fourth-order peaks at the positions expected for a hexagonal phase (ratios 1, $\sqrt{3}$, $\sqrt{4}$, and $\sqrt{7}$). All of these features indicate an increase in the degree of ordering as time proceeds. From the main peak position we determine the lattice constant to be $a=6.15$ lattice units. Characteristic length scales for the average microdomain size can be

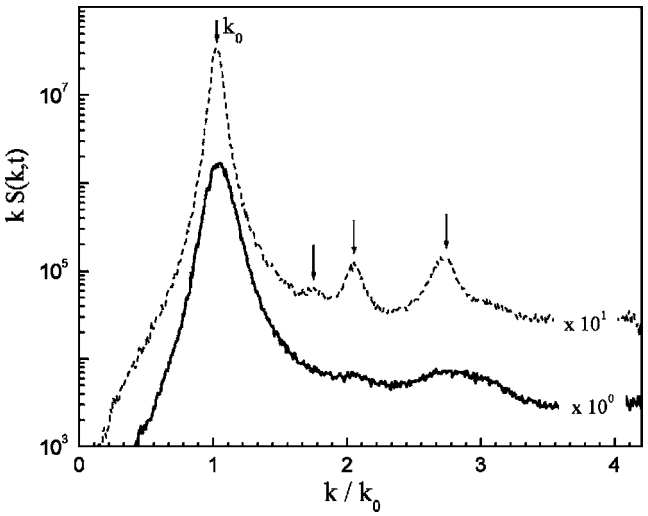

FIG. 1. Circularly averaged scattering function $S(k)$, multiplied by the wave vector k, at two different times (short time, continuous line; long time, dotted line). The pattern corresponding to long times was vertically shifted by a factor of 10. The arrows indicate the peak positions corresponding to a hexagonal phase.

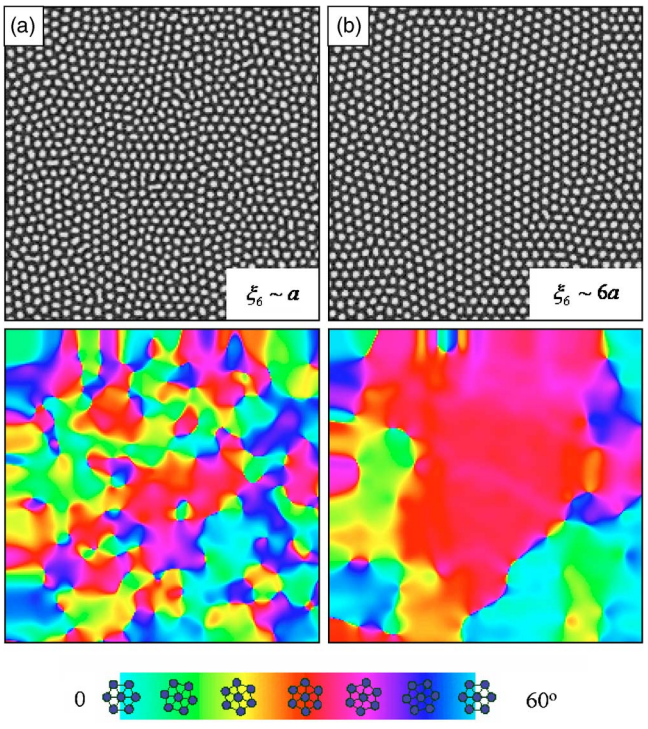

FIG. 2. (Color online) Patterns and orientational maps obtained at different simulation times. The patterns on the left panel correspond to short times (10^3 time steps) and on the right to long times (10^5 time steps). The bottom of the figure shows the gray scale (color scale) used to indicate orientation.

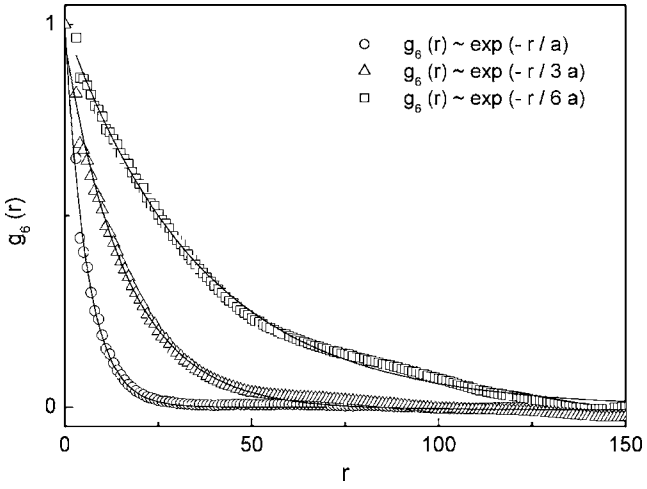

FIG. 3. Orientational correlation functions at three different times. Squares correspond to the orientational correlation function of the pattern depicted on the right side of Fig. 2. The continuous lines represent single exponential fits.

obtained through the full width at half maximum of the main peak of $S(k,t)$ as $\xi_S \sim \delta S_{HW}(t)^{-1}$ [24].

The orientational correlation function for a system with hexagonal symmetry is defined as [11,24]

$$g_6(r,t) = \langle \exp\{6i[\theta(\vec{r}+\vec{r}',t) - \theta(\vec{r}',t)]\}\rangle \qquad (15)$$

where $\theta(\vec{r})$ is the local intersphere "bond" orientation, determined in real space by a Delaunay triangulation through the center of the spheres. More details about the data processing can be found elsewhere [11]. Recently, Yokojima and Shiwa have used another method to determine the orientational field $\theta(\vec{r})$ [24]. Instead of calculating the orientational field in real space these authors have employed a Fourier space filtering method to study the influence of hydrodynamic interactions on the scattering function and orientational correlation function. A filtering operator (Gaussian) is applied to reduce the amplitude of the components of $\tilde{\psi}(\vec{k},t)$ that lie outside a ring centered around the main peak of $S(\vec{k},t)$. Note that although it is computationally simple, this method has the disadvantage of smearing the orientational field. As a consequence, very interesting features of the patterns, such as grain boundaries, can be modified by the filtering process. In addition, such a filtering procedure may artificially increase the orientational order in the system. The lower panels in Fig. 2 show gray-scale (color) maps of the orientational field for the same images at the top in Fig. 2, with the gray-scale (color) key (shown at the bottom in Fig. 2) indicating the orientational field over the range $[0,\pi/3]$, as appropriate for a sixfold symmetric structure. Through the gray-scale (color) map, regions with similar orientation can be identified easily.

Figure 3 shows the orientational correlation function obtained from the orientational field at three different times. The roughly exponential decay of the orientational correlation function allows us to define an orientational correlation length ξ_6 as

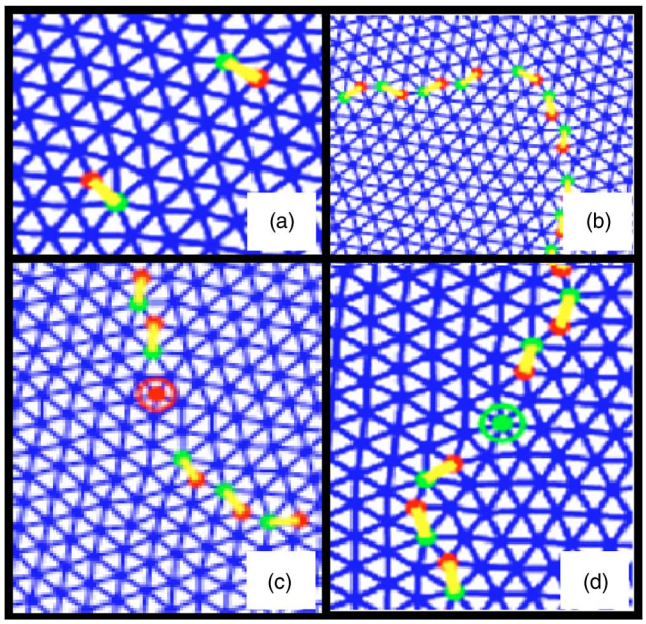

FIG. 4. (Color online) Defects analyzed in this work. Spheres with seven neighbors are indicated with a light gray (green) dot, those with five neighbors in dark gray (red). (a) Dislocations are formed by a pair of 5-7 disclinations separated by one lattice constant, and are indicated by a connecting pale gray (yellow) line segment. (b) Linear array of dislocations delimiting a grain boundary. (c) and (d) shows disclinations bound to a LAGB.

$$g_6(r,t) \sim \exp\left[-\frac{r}{\xi_6(t)}\right]. \qquad (16)$$

In Fig. 3 the circles and squares represent the short- and long-time correlation functions corresponding to the two patterns shown in Fig. 2, respectively. At short times, the orientational correlation length is approximately one lattice constant ($\xi_6 \approx a$), and both translational and orientational correlation lengths are short ranged (see also Fig. 1 and the left panels of Fig. 2). At long times (see Fig. 1 and the right panels of Fig. 2), the greater ordering is evidenced through the increase in the orientational correlation length ($\xi_6 \approx 6a$).

It is important to emphasize that the exponential decay in the orientational correlation function found here is not related to the Kosterlitz-Thouless-Halperin-Nelson-Young (KTHNY) theory [26,27]. According to the KTHNY theory, above the characteristic temperature at which the hexatic phase becomes unstable, both translational and orientational correlation lengths are short ranged and decay exponentially with distance. However, the KTHNY theory is a model for a system in complete thermodynamic equilibrium, while the system studied here is far from equilibrium.

IV. FEATURES OF THE PATTERNS

The features of the patterns and degree of ordering strongly reflect the presence of topological defects. To understand the evolution of the pattern, it is essential to know the topological defects present in the system, as well as their influence on the ordering process. In addition to the orienta-

tional map, through the Delaunay triangulation it is possible to determine the number of dislocations and disclinations in the system [11]. For the hexagonal phase, dislocations are defined as pairs of spheres with five and seven nearest neighbors separated by a lattice constant [27]. Disclinations are identified as "free," rather than bound into a dislocation, if all the nearest neighbors are free of defects, or engaged in other dislocations.

Figure 4 illustrates the different kinds of defects analyzed in this work. In Fig. 4(a) we show a hexagonal lattice containing two dislocations with similar orientations but opposite Burgers vectors. Note that each dislocation introduces two extra "lines" in the hexagonal array. Here we indicate defects with five neighbors in dark gray (red), and those with seven neighbors in light gray (green). Dislocations are indicated as pale gray (yellow) line segments uniting nearest-neighbor "fives" and "sevens." In Fig. 4(b), we show a line of dislocations delimiting two grains with a large-angle grain boundary (LAGB). The largest possible mismatch in orientation for our patterns is 30°; thus, we define a "large-angle" grain boundary as one with an orientational mismatch in the range 10°–30°. Unpaired disclinations ("fives" and "sevens") are highlighted by circling the defect with a range of the same gray level (color). Figures 4(c) and 4(d) show lines of dislocations with bound disclinations.

Figure 5 shows the results of a Delaunay triangulation on a pattern at a late stage of coarsening. This figure corresponds to a small portion of a larger picture (obtained through a 1024×1024 simulation). Figure 6 shows the orientational map corresponding to Figure 5; three specific grains are labeled in both figures, to facilitate comparison. These and other patterns present the following recurring

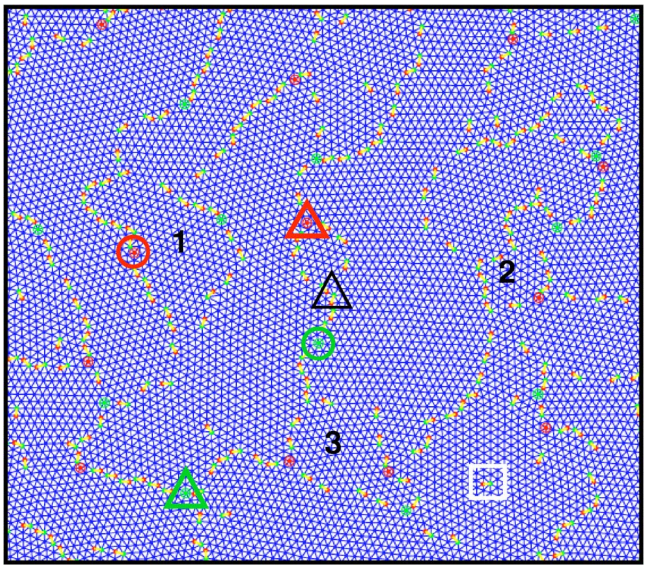

FIG. 5. (Color online) Delaunay triangulation of the pattern at a late stage of coarsening. Light gray (green) and dark gray (red) triangles indicate forks containing positive and negative disclinations, respectively. The black triangle (thin line) indicates a fork free of disclinations. Light gray (green) and and dark gray (red) circles indicate positive and negative disclinations located on LAGBs. The white square indicates a "free" dislocation, located in the interior of a relatively well-defined grain.

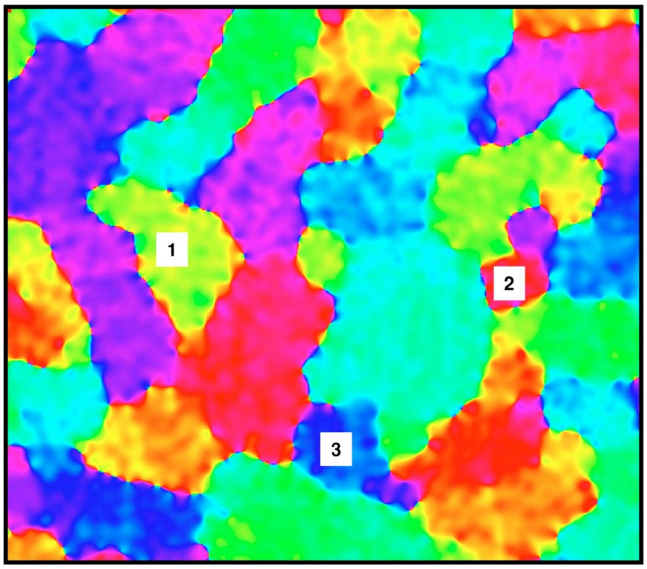

FIG. 6. (Color online) Orientational map of the pattern shown in Fig. 5. The gray (color) scale is the same as in Fig. 2.

characteristics. (1) Most of the grain boundaries are LAGBs, consisting of lines of dislocations. Although small-angle grain boundaries (SAGBs) can also be observed in Fig. 5, their population is clearly smaller. (2) In many cases, the grains do not have well-defined contours. This is more clearly visualized in the gray-scale (color) map of Fig. 7, which shows another region of the simulation depicted in Figs. 5 and 6. In Fig. 7, we have labeled four "grains" with letters A through D. The A/B and B/C grain boundaries cannot be clearly defined, in contrast with the sharp transition in the orientational field between grains B and D. For SAGBs, the distance between dislocations grows as a/θ, where θ (in radians) represents the mismatch in orientation between two adjacent grains [27]. Note that for small angles, the distance a/θ can become comparable to the characteristic distance between LAGBs; in that case, a SAGB cannot be defined as a line of dislocations in a polycrystal. (Obviously, in a system consisting of only two grains, a SAGB can be defined as a line of dislocations simply by considering grains "large enough" that their boundaries involve many disloca-

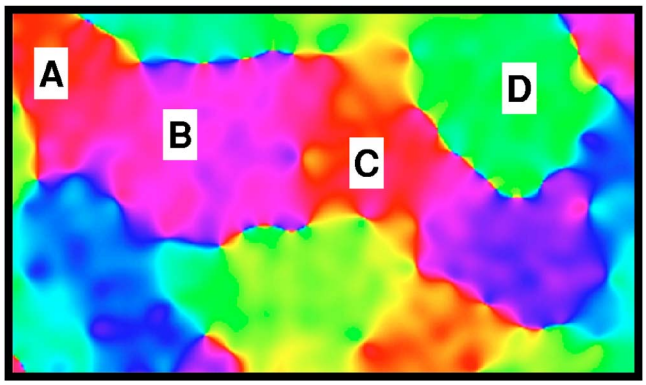

FIG. 7. (Color online) Gray-scale (color) map depicting the difficulties in locating SAGBs. Note the fluctuations in the orientational field. The gray (color) scale is the same as in Fig. 2.

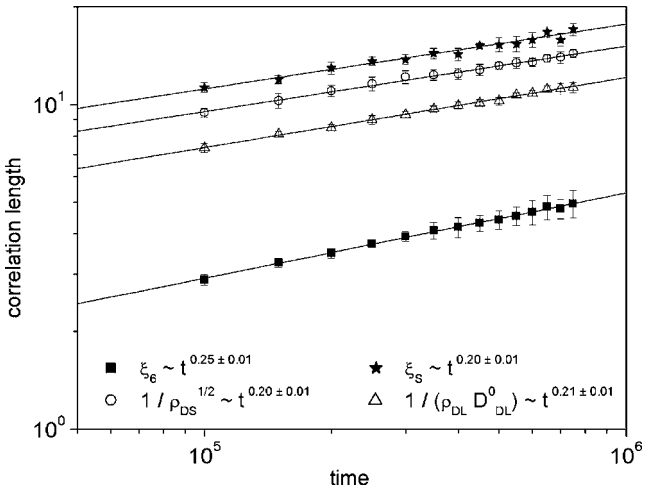

FIG. 8. Different correlation lengths analyzed in this work (indicated in the figure), and best-fit power laws (solid lines).

tions. Thus, in the polycrystal, there is really no distinction between an isolated dislocation and one on a grain boundary having such a small angle that only one dislocation will be present along its length). In the interior of large grains, it is possible to observe a small amount of "free" dislocations. In Fig. 5, we have indicated the presence of one of these "free" dislocations with a white square; there is no clear way to identify which grain boundary this dislocation belongs to, if any. (3) In the interior of the grains it is possible to visualize small fluctuations in the orientational field, indicating the presence of orientational distortions (Figs. 6 and 7). These fluctuations are expected to reduce the translational correlation length. However, the fluctuations would have little influence on the orientational correlation length. (4) There are no free disclinations; all the disclinations present in the system are bound to LAGBs. In Fig. 5 we have emphasized the presence of a few representative disclinations; most are bound to "forks," where grain boundaries bifurcate, as indicated in Fig. 5 with light gray (green) and dark gray (red) triangles. There is also a small population of disclinations located on grain boundaries, but not at forks, indicated in Fig. 5 with circles. Note, however, that not all forks contain disclinations; one such fork is indicated in Fig. 5 with a black triangle.

V. GROWTH LAWS FOR CORRELATION LENGTHS

Figure 8 shows the temporal evolution of the correlation length $\xi_S(t)$ and orientational correlation lengths $\xi_6(t)$ (here t represents the number of time steps). The results reported in this figure correspond to an average of six different runs. While both correlation lengths scale with time according to a power law, we find different exponents in the two cases: $\xi_S(t) \sim t^{1/5}$, while $\xi_6(t) \sim t^{1/4}$. Recently, by using cell dynamics simulations, Yokojima and Shiwa [24] found exponents of 0.17 for $\xi_S(t)$ and 0.2 for $\xi_6(t)$. In their simulations these authors use a slightly different model and parameters, and their simulations do not include random fluctuations (i.e., $\eta = 0$); nonetheless, Yokojima and Shiwa also find slightly smaller exponents for $\xi_S(t)$ than for $\xi_6(t)$.

Previous experimental results from our group on monolayers of cylinder-forming block copolymers clearly showed that the orientational correlation length is dominated by the annihilation of topological defects [8,10]. We also found a remarkable decrease in the density of topological defects during the simulated coarsening process. This result suggests that in a hexagonal system, the orientational correlation length may also be determined by the interaction between topological defects. To establish the relationship between correlation lengths and topological defects, it is important to track the temporal evolution of the defects during the coarsening process.

Close inspection of the coarsening process indicates that the main mechanism of coarsening proceeds via grain annihilation. If grain rotation is frustrated during the coarsening process, the ratio between grain size and number of dislocations clustered along the grain remains roughly constant. Assuming that the average grain radius is R, then the number of dislocations on the grain boundary scales as $\rho_{DL}R^2$, where ρ_{DL} is the dislocation density. If the average distance between dislocations D_{DL} remains constant during the annihilation (i.e., no grain rotation) then the number of dislocations per grain scales as R/D_{DL}. Comparing, we have or $\rho_{DL}R^2 \sim R/D_{DL}$ or $R \sim [D_{DL}\rho_{DL}]^{-1}$. Then, if the orientational correlation length $\xi_6(t)$ is dominated by the density of dislocations (observe Fig. 5) and D_{DL} remains constant, the orientational correlation length should evolve as $\xi_6(t) \sim [D^0_{DL}\rho_{DL}(t)]^{-1}$, where D^0_{DL} is the characteristic distance between dislocations.

Figure 8 also shows $[D^0_{DL}\rho_{DL}(t)]^{-1}$ as function of time. The average distance between dislocations along LAGBs was observed to have a roughly constant value of $D^0_{DL} = 2.5a$; assuming that the SAGB approximation is valid, this value of D^0_{DL} corresponds to a misorientation of 20°, which is close to the observed average misorientation between grains. Observe in Fig. 8 that although $[D^0_{DL}\rho_{DL}(t)]^{-1}$ is also well described by a power law, the exponent is smaller than the exponent corresponding to the orientational correlation length ($[D^0_{DL}\rho_{DL}(t)]^{-1} \sim \rho_{DL}(t)^{-1} \sim t^{0.2}$ vs $\xi_6(t) \sim t^{0.25}$). This may indicate a residual contribution coming from a decrease in the average distance between dislocations, i.e., $D_{DL} \sim t^{-0.05}$ instead of $D_{DL} = D^0_{DL} = \text{const}$, which may indicate either preferential annihilation of SAGBs or grain rotation, as discussed further below.

On the other hand, if coarsening is dominated by the annihilation of disclinations, as in the case of smectics [8], we may expect that $\xi_6(t) \sim \rho_{DL}^{-1/2}$, where ρ_{DS} represents the density of disclinations. Figure 8 also shows the evolution of this quantity, which also follows the power law $\rho_{DS}^{-1/2} \sim t^{0.2}$. Thus, for the hexagonal system studied here we have $\xi_S(t) \sim \rho_{DL}^{-1} \sim \rho_{DS}^{-1/2} \sim t^{0.2}$, which suggests that these correlation lengths are controlled by similar mechanisms. However, the higher exponent for $\xi_6(t)$ indicates that a different process must be affecting the orientational order. These results are in very good agreement with the recent measurements of Harrison *et al.*, which show similar characteristics [11].

VI. GRAIN ROTATION IN CIRCULARLY SYMMETRIC GRAINS

To test the possibility of grain rotation, we prepared an initial configuration consisting of a circular misoriented grain

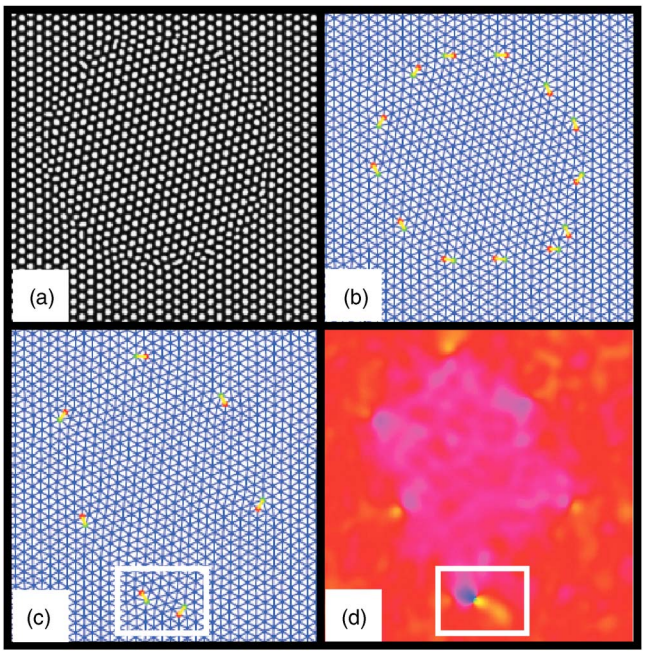

FIG. 9. (Color online) Circular misoriented grain in the interior of a larger one. (a) Hexagonal pattern containing a circular grain with a 10° orientational mismatch. (b) Corresponding line of dislocations along the grain boundary. (c) Line of dislocations for an originally circular grain with a 5° orientational mismatch. (d) Gray-scale (color) map corresponding to (c) (observe the fluctuations in orientation at the bottom of the "grain"). The gray (color) scale is the same as in Fig. 2.

surrounded by an otherwise perfect crystal (neglecting boundary defects produced by the cyclic boundary conditions). To obtain the initial configuration, we employed the wave vector $\vec{k}_0$ determined through the main peak of the scattering function of a pattern obtained from a randomly disordered initial condition at a late stage of coarsening. The external crystal was obtained by using the following initial condition in Eq. (8):

$$\psi_i(\vec{r}) = \tfrac{1}{2}\psi_0 \sum_{j=1}^{3} (e^{\vec{k}_j \cdot \vec{r}} + \text{c.c.}). \tag{17}$$

Here ψ_0 is the initial amplitude and $\vec{k}_1=(k_0,0)$, $\vec{k}_2=(-k_0, -\sqrt{3}/2k_0)$, and $\vec{k}_3=(-k_0,\sqrt{3}/2k_0)$ are the wave vectors corresponding to a hexagonal pattern. The circular grain was also obtained through Eq. (17), but employing a wave vector rotated to the desired angle.

Figure 9(a) depicts a circular grain with a misorientation of 10° at early times (10^4 time steps) and without random fluctuations ($\eta=0$); note the ill-defined spheres and defects at the interface. Figure 9(b) shows the array of dislocations around the grain depicted in Fig. 9(a); the dislocations are evenly distributed along the grain boundary. In the absence of random fluctuations, beyond about 10^4 time steps the shape and size of the misoriented grain remain roughly constant, even after a large number of time steps (10^6). Some simulations showed facets with well-defined orientation, revealing the influence of the anisotropy in the "surface" tension. Facets were found at different misorientations of the circular grain, ranging from 10°–30°.

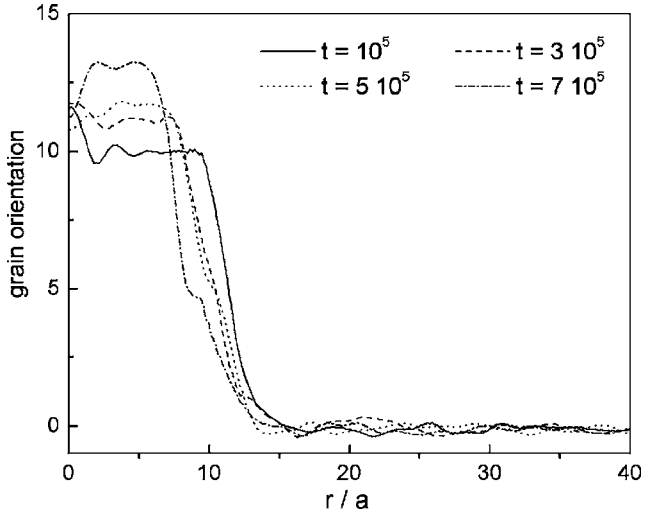

FIG. 10. Grain orientation as function of distance from the center at four different times. The initial orientational mismatch of the circular grain was 10°.

When random fluctuations are added, the motion of the interface is activated and the grain collapses. Figure 10 shows the circularly averaged local orientation as a function of the distance from the center of the circle (in units of a). The initial mismatch in orientation between both grains is 10°. Figure 10 shows that the orientational mismatch increases with time, while the domain size decreases. During the process depicted in Fig. 10, the number of dislocations remains constant, indicating that the distance between dislocations has been reduced ($D_{DL}\sim a/\theta$).

Figure 11 shows the temporal evolution of the average grain orientation $\theta(t)$, the average distance between dislocations D_{DL}, and the average grain size $\langle R\rangle$. The average grain orientation was determined by fitting the circularly averaged orientation with a sigmoid (Boltzmann). The grain size was obtained as the value of R at which the orientation changes by $\theta/2$. The average distance between dislocations was obtained by taking the average distance between nearest-neighbor dislocations. Figure 11 shows that all of these quantities grow following power laws with similar exponents: $\theta(t)\sim D_{DL}^{-1}\sim\langle R\rangle^{-1}\sim t^{0.1}$, in agreement with the SAGB approximation. Let $N_{DL}\sim\langle R\rangle/D_{DL}$ be the number of dislocations along the grain boundary; then, $\langle R\rangle$ can be related to $\theta(t)$ through $\langle R\rangle\sim N_{DL}D_{DL}(t)\sim N_{DL}\theta(t)^{-1}$, or $\langle R\rangle\sim D_{DL}(t)\sim\theta(t)^{-1}$, because N_{DL} remains constant during the grain shrinking process depicted in Figs. 10 and 11. Note that although N_{DL} remains constant during the time window depicted here, this is not generally the case; since θ has a finite upper bound of 30°, once the misorientation becomes close to 30°, grain shrinking must proceed via annihilation of dislocations.

This result appears to be at odds with the coarsening model recently proposed by Moldovan *et al.* [28], where coarsening involves the coordinated rotations of neighboring grains with the consequent elimination of their common grain boundary (i.e., θ is a decreasing function of time).

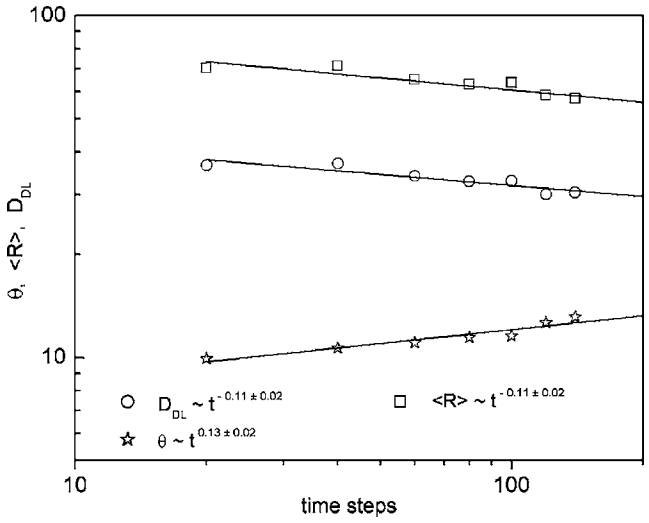

FIG. 11. Orientation, average grain size, and average distance between dislocations along the grain boundary as function of time. The symbols are indicated in the figure and the lines correspond to best-fit power laws.

According to the Read-Shockley formula, the energy per unit of length of a small-angle grain boundary is given by [27]

$$\gamma(\theta) \sim \theta[1 - \delta \ln(\theta)] \tag{18}$$

where θ is the misorientation angle across the grain boundary (expressed in radians) and δ is a constant related to the core energy of the dislocation. This model is based on a dislocation structure; for three-dimensional crystals, experimental data show that $\gamma(\theta)$ has a maximum for θ in the range 30°–40°. So, in our case, according to the approximation given by Eq. (18), the energy density $\gamma(\theta)$ increases during the shrinking; however, the total surface energy $[\sim R\gamma(\theta)]$ decreases because the grain becomes smaller as rotation proceeds. Note also that the growth law for $\theta(t)$ determined for this particular misorientation does not agree with our previous scaling laws for $\xi_6(t)$ or $\xi_S(t)$ starting from a random initial condition. This demonstrates that the dynamics of individual grain boundaries depend strongly on both $\gamma(\theta)$ [27] and "rotational mobility" [28], which are functions of the misorientation angle.

In simulations with small misorientations ($\theta \sim 5°$), the dynamics of coarsening appear to be different. Figures 9(c) and 9(d) show the results of a simulation for a circular grain with $\theta = 5°$. If the mismatch in orientation is small, the number of dislocations is not conserved during the rotation; different regions of the grain can rotate to cancel the local mismatch in orientation. In this case, the rotation is accomplished by moving dislocations from regions where they are widely spaced toward regions with a higher concentration of dislocations. The annihilation events are produced in the small regions where the density of dislocations is large. This characteristic can be observed in the region contained within the white rectangle at the bottom of Figs. 9(c) and 9(d); note the small distance between dislocations, and the distortions in the orientational field in this region. We also have observed that the mobility of such dislocations is higher than the mobility of dislocations linked to LAGBs, as discussed further below. In the case of small misorientations, it is difficult to characterize the temporal evolution of the "grain size" through the same parameters as for LAGBs, for

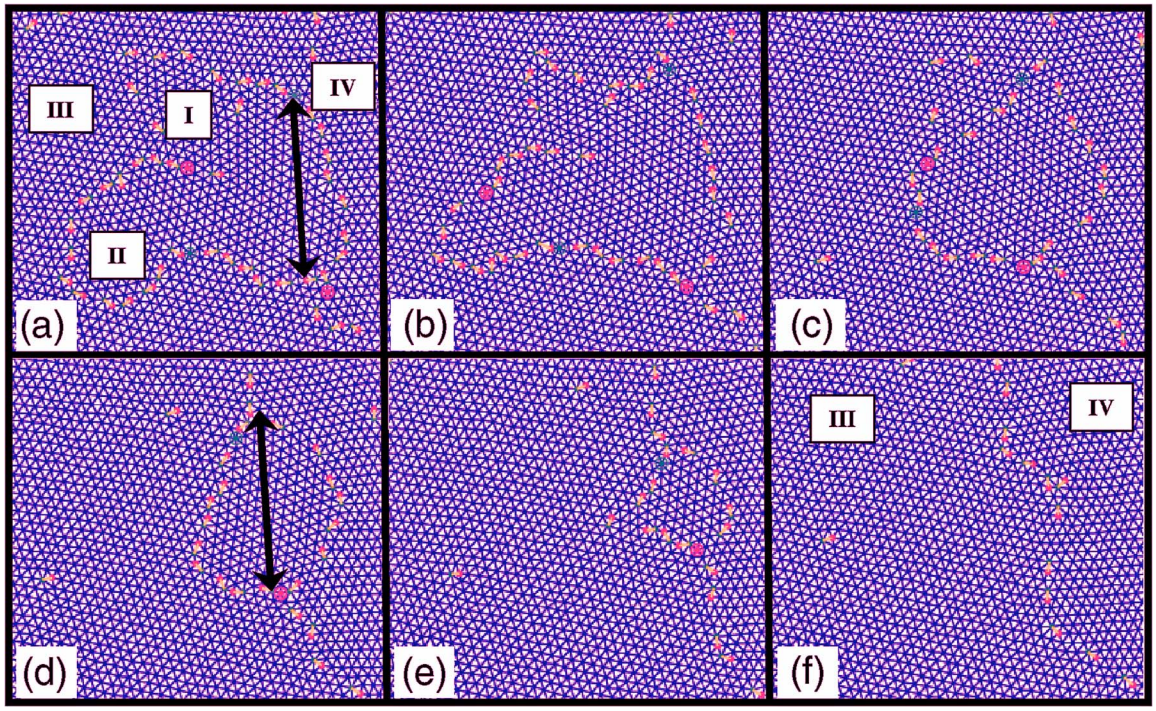

FIG. 12. (Color online) Main mechanism of coarsening observed in the simulations: the collapse of small grains lying on the boundaries of large grains.

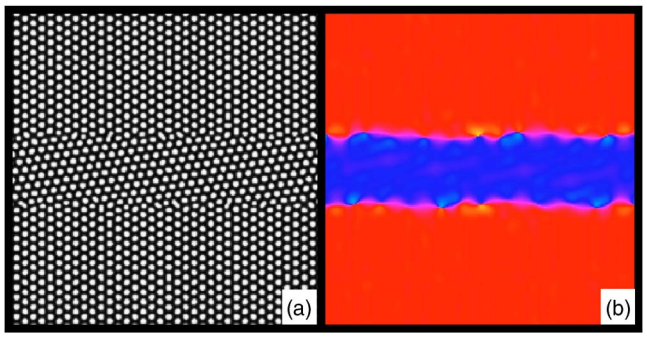

FIG. 13. (Color online) Misoriented grain with straight grain boundaries. The difference in orientation between both grains is 20°. (a) Array of spheres. (b) Orientational gray-scale (color) map (scale same as in Fig. 2).

three reasons: (1) the grain contour is ill defined, (2) the dislocations are not uniformly distributed along the grain boundary, and (3) the change of orientation is not circularly (polar) symmetric, as shown in Fig. 9(c).

VII. MECHANISM OF COARSENING

The temporal evolution of the patterns reveals that the bounded disclinations move easily along dislocation lines, while spending most of their time at the forks, as shown in the snapshot of Fig. 5. Although coarsening involving only one grain (the collapse of loops) or more than three grains has been observed, the main mechanism of coarsening at LAGBs is the annihilation of small grains located at the intersections of larger grains. This mechanism of annihilation is illustrated in the sequence of Fig. 12. In Fig. 12(a), two smaller grains (indicated as I and II in the figure) are seen in the "sea" formed by two larger grains (III and IV). Figure 12(b) shows the shrinking of the two smaller grains at longer times. Figures 12(c) and 12(d) show the collapse of grain I and the shrinking of grain II. During this process, the distance between the forks indicated with the black arrow in Fig. 12(d) remains essentially the same as in Fig. 12(a) (although there are fluctuations around their average positions). In the subsequent Figs. 12(e) and 12(f), we observe the complete annihilation of grain II, located at the intersection of the two larger grains.

This process of coarsening is markedly different from that observed in other systems; such as coarsening is driven by curvature. During the process of grain annihilation, the motion of dislocation lines (LAGBs) appears to be independent of the presence of other dislocation lines, except at the forks. The color maps for the orientational fields indicate that the distortions introduced into the lattice by lines of dislocations decay to negligible values in a few lattice constants, i.e., the strain field appears to be strongly screened (see discussion below). Only if the distance between two roughly parallel dislocation lines becomes comparable to one lattice constant, can the dislocations glide recombine or annihilate with others of opposite sign. This certainly happens at the forks, where two dislocation lines merge to a point and can be roughly parallel to each other.

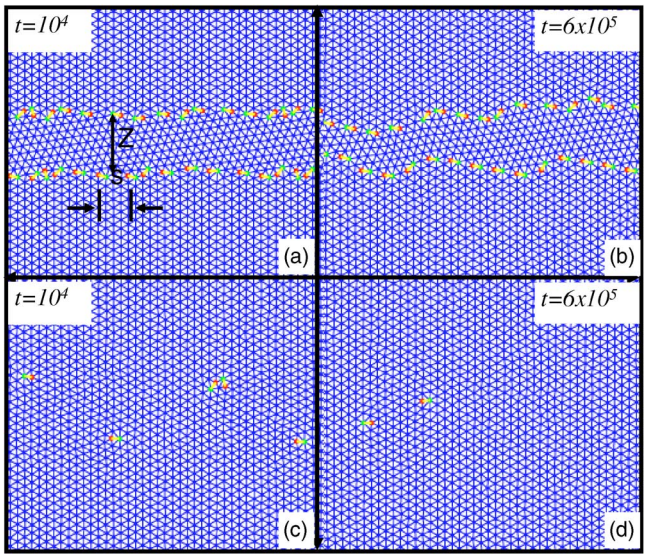

FIG. 14. (Color online) Delaunay triangulation for misoriented grains with straight grain boundaries at the two different simulation times, as indicated in the figure. The top panels have an initial misorientation of 20°, those at the bottom 2.5°.

The motion of the forks appears to be activated by motion of the dislocation lines. If the effects of anisotropy are small, when the angle between dislocation lines at the fork is 120°, the net force on the fork is null and the fork is pinned at its position. On the other hand, if one of the angles between two of the three lines merging at the fork is strongly reduced below 120°, a net force acts on the fork. However, to activate the motion of the fork, the potential barriers imposed by the lattice and dislocation lines must be overcome. In Fig. 12 this activation appears to be triggered by the annihilation of the smaller grain. Once the fork motion is activated, the grain shrinkage accelerates, and the small grain collapses with a roughly elliptical self-similar shape [compare the grain's shape in Figs. 12(d) and 12(e)], with the forks located along the major axis of the ellipse. To keep the self-similar shape, the velocity of displacement of the fork must be greater than the speed of dislocations located near the minor axis of the ellipse.

In the absence of external fields, two dislocations with Burgers vectors $\vec{b}_1$ and $\vec{b}_2$ interact with each other with a long-range potential of the form

$$V = -\frac{K}{4\pi}\left[\ln|\vec{r}_1 - \vec{r}_2|\vec{b}_1 \cdot \vec{b}_2 - \frac{\vec{b}_2 \cdot (\vec{r}_1 - \vec{r}_2)\vec{b}_1 \cdot (\vec{r}_1 - \vec{r}_2)}{|\vec{r}_1 - \vec{r}_2|^2}\right] \tag{19}$$

where K is a function of the elastic constants. From this functional relation, it is possible to calculate the energy U associated with a pair of parallel lines of dislocations (grain boundaries) with opposite Burgers vectors. If the distance between grain boundaries is z, the energy density becomes short ranged and has the form [29]

$$U(z) = \frac{1}{s}\frac{K}{4\pi}\left\{\ln\left[\sinh\left(\frac{\pi z}{s}\right)\right] - \frac{\pi z}{s}\coth\left(\frac{\pi z}{s}\right) + \ln\left(\frac{s}{\pi}\right)\right\} \tag{20}$$

where s is the distance between dislocations. Although in our case the dislocation lines are curved rather than straight, we can expect that the strain field introduced by dislocations located along LAGBs also becomes screened at large distances, but we do not expect any significant screening at distances lower than s ($\approx a$ for a LAGB).

The situation changes for dislocations located along SAGBs. Let R_{LA} be the average size of a grain defined exclusively by the LAGB. As we mentioned previously, in the interior of such grains it is possible to have fluctuations in orientation and a small number of "free" dislocations; we can expect that the strain field surrounding these interior dislocations is poorly screened by other dislocations, since few will be located at distances lower than R_{LA}. Consequently, a higher mobility for such "free" dislocations is expected.

To test the effect of screening, we ran simulations from the type of initial condition depicted in Fig. 13, involving two grains (misoriented by 20° in Fig. 13), with a straight grain boundary. Figures 14(a) and 14(b) show the results after 10^4 and 6×10^5 time steps, respectively; Figs. 14(c) and 14(d) show analogous results for the case where the initial misorientation angle was only 2.5°. In Fig. 14(a) the average distance between dislocations along the grain boundary is $1-2a$, while the distance between the dislocation lines is $6a$. In Fig. 14(c), the average distance between dislocations is $23a$, while the distance between the dislocation lines remains $6a$. In the case of LAGBs, at long times the dislocation lines undulate [Fig. 14(b)]. Although it is possible to observe dissociation and recombination of dislocations, the number of dislocations is roughly conserved during this stage. In addition, the motion of individual dislocations is strongly pinned to the grain boundary and dislocations cannot move more than a few lattice spacings away; the diffusion of dislocations to larger distances can be accomplished only through the cooperative motion of the line of dislocations.

At times longer than those in Fig. 14(b) (around 10^6 time steps, not shown here), as a consequence of the undulations, the dislocation lines with opposite Burgers vectors touch each other, annihilate some dislocations, and form small "drops." As time proceeds, these drops shrink and collapse individually. On the other hand, when the distance between dislocations along the grain boundary becomes larger than the distance between grain boundaries [Figs. 14(c) and 14(d)], the situation is very different. In this case the strain field of the individual dislocations has a range larger than the distance between grain boundaries. Compared with dislocations bound to LAGBs, this yields a higher mobility for the dislocations; note in Figs. 14(c) and 14(d) the annihilation of dislocations and the decrease in the average distance between the two remaining ones. These defects speed up the coarsening process because they can move over large distances (many lattice constants) in a relatively reduced number of time steps.

The patterns studied here are dominated by the presence of LAGBs, which may be a consequence of the preferential annihilation of SAGBs or/and grain rotation. From the two possible mechanisms proposed here, we favor the selective annihilation of SAGBs. According to our previous discussions, to have an orientational correlation length dominated exclusively by dislocations, the interdislocation distance must decrease as $D_{DL}\sim t^{-0.05}$. Under the small-angle approximation this implies the unexpected result of grain rotation towards increasing misorientation. Since $D_{DL}\sim a/\theta$, by imposing $\xi_6(t)\sim[D_{DL}\rho_{DL}]^{-1}$ we must have θ growing with time as $\theta\sim t^{0.05}$. Since the misorientation angle has an upper bound of 30°, the power law for $\xi_6(t)$ cannot remain valid at long times. Then, if grain rotation is the mechanism responsible for the 1/4 exponent in $\xi_6(t)$, in the long-time regime this power law must break down and $\xi_6(t)$ must become parallel to $1/\rho_{DL}$ (exponent 1/5). Although we have observed grain rotation in circularly symmetric grains in the previous section, in the case of polycrystals each grain is surrounded by other grains with different orientations and grain rotation is expected to be highly frustrated. On the other hand, for the preferential annihilation of SAGBs, there is no limitation on the time scale for validity of the power law for $\xi_6(t)$, and the results are in good agreement with the observations, i.e., high mobility of dislocations located along SAGBs and patterns dominated by the presence of LAGBs.

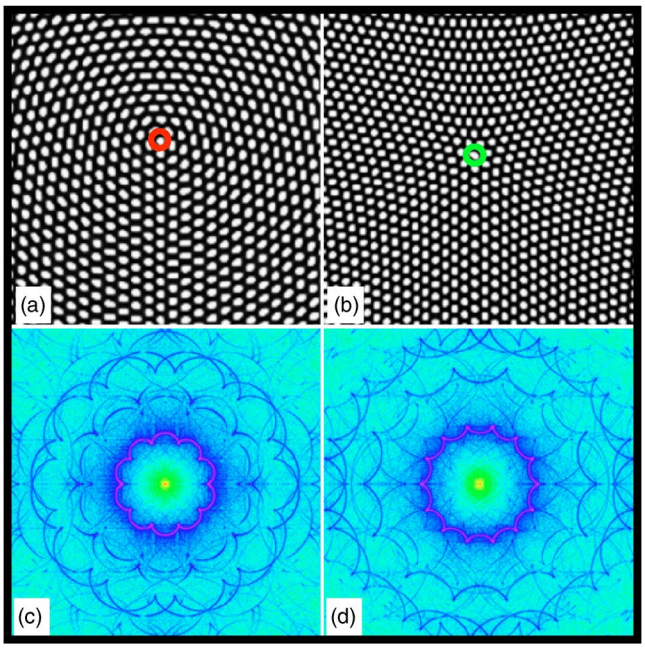

FIG. 15. (Color online) Negative (left) and positive (right) disclinations and the corresponding two-dimensional Fourier transform (bottom). The gray (color) scale is the same as in Fig. 2.

VIII. DISCLINATIONS

In our simulations we have not found free disclinations; all disclinations were bound to LAGBs, most commonly at the forks. To analyze the stability of free disclinations we prepare an artificial starting condition with free positive and negative disclinations [Figs. 15(a) and 15(b)]. In the absence of random fluctuations, the patterns for both disclinations

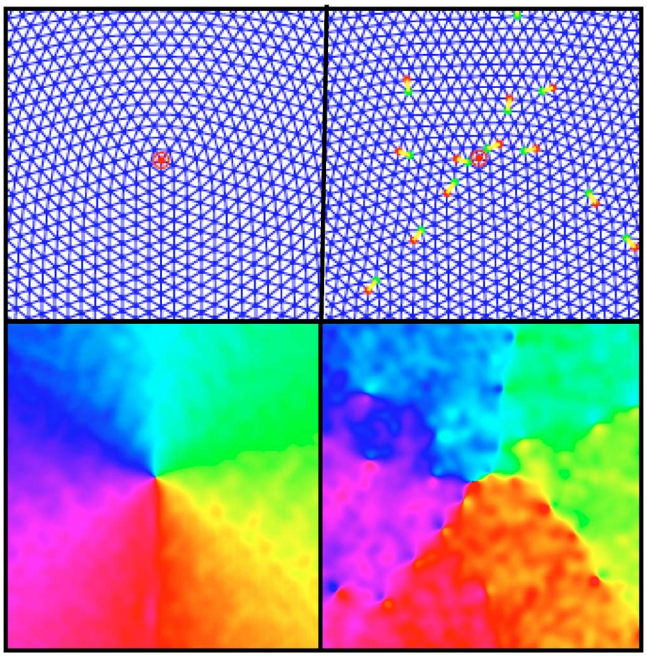

FIG. 16. (Color online) Top: Delaunay triangulation for a negative disclination in the absence (left) and presence (right) of random fluctuations. Bottom: orientational color maps corresponding to the figures on top, with the gray (color) scale the same as in Fig. 2.

remain stable, even after a large number of time steps. Observe in Fig. 15 that the domains are strongly stretched as consequence of the strain field introduced by the disclination. This highlights an important difference between the behavior of block copolymers and simulations of other types of materials, such as arrays of atoms interacting via Lennard-Jones potentials [30]. In atomistic simulations the shape of the elementary units is not perturbed by the strain field. Here, however, the polymer chains can stretch to change the shape of the microdomains.

In Figs. 15(c) and 15(d) we show the scattering function for these same two disclinations. Instead of the hexagonally ordered spots observed for monocrystals with hexagonal symmetry, we find a flowerlike pattern, with a number of "petals" revealing the symmetry of the disclinations: 10 petals for a negative disclination (a "five") and 14 "inverted petals" for a positive disclination (a "seven"). As a consequence of the strain, there is broad range of characteristic distances and the circularly averaged scattering functions do not present a simple structure like those in Fig. 1. Note also that in the presence of disclinations, both orientational and translational correlation functions become short ranged.

When random fluctuations are included in the simulations, the disclination strain field quickly becomes disturbed by dislocations, as shown in Fig. 16 for a negative disclination; similar results were found for positive disclinations. Most of the dislocations are arranged in lines radiating from the core of the original disclination, and the strain originally present in the disclination has been strongly reduced by the dislocation lines, making the strain field of the disclination short ranged. During this process, the microdomains recover roughly circular symmetry. Dislocation lines radiating from a disclination core have also been observed in two-dimensional Lennard-Jones systems at equilibrium [30].

IX. COMPARISON WITH EXPERIMENTAL DATA

By comparing our simulations with recent experimental results of Harrison *et al.* [11] we find, in general, very good agreement. Both experiments and simulations show higher exponents in the power laws for $\xi_6(t)$ than for $\rho_{DL}^{-1}(t)$ or $\rho_{DS}^{-1/2}(t)$, and the differences between exponents (~ 0.05) is consistent. In addition, there are a number of points where the similarity is remarkable: (1) there are no free disclinations; all are bound to LAGBs; (2) most of the dislocations are contained in LAGBs; (3) in many cases grain boundaries are ill defined, and there are fluctuations in the orientational field; (4) dislocation pairs are annihilated at the forks by the gliding of two roughly parallel dislocations; and (5) the dynamics of coarsening are dominated by the collapse of small grains located at the intersection of two larger grains.

CONCLUDING REMARKS

In this work, we have used cell dynamics simulations to analyze the features and the mechanism of coarsening in the two-dimensional patterns present in single-layer films of a sphere-forming block copolymer. We have tracked the time evolution of the orientational correlation length, and correlation lengths determined through densities of topological defects and from scattering functions. Simulations with predefined, straight LAGBs indicate that the strain field surrounding lines of dislocations is short ranged. This explains why a dislocation line moves independently and interacts with others mainly at the forks, where the distance to dislocations belonging to other lines becomes very small. In addition, we have observed that the strain field associated with isolated dislocations, or those in SAGBs, is poorly screened. As a consequence the dislocations can move over large distances to find a partner with opposite Burgers vector and annihilate. This also explains why the patterns show a large population of LAGBs.

All disclinations are located in LAGBs, predominantly at the forks. The strain field of these disclinations is short ranged and appears to have no effect on the orientational order. Simulations starting from isolated positive or negative disclinations reveal that they are strongly unstable, and the strain field quickly becomes relaxed by the spontaneous creation of dislocation lines radiating from the disclination.

One of the most important results of this work is the higher exponent in the power law observed for $\xi_6(t)$ than for the other correlation lengths [ρ_{DL}^{-1}, $\rho_{DS}^{-1/2}$, or $\xi_S(t)$], in agreement with the experimental results of Harrison *et al.* [11]. The difference in the exponents can arise from either grain rotation or preferential annihilation of SAGBs; we favor the selective annihilation of SAGBs, as in this case the power laws observed in both simulations and experiments are not limited in the time scales over which they are valid. Finally, cell dynamics simulations are shown to be a very important tool for understanding the basic mechanisms of coarsening of these types of soft materials.

ACKNOWLEDGMENTS

This work was supported by the National Science Foundation through the Princeton Center for Complex Materials (Grant No. DMR-0213706). We gratefully acknowledge useful discussions with S. T. Milner. D.A.V. gratefully acknowledges support from the National Research Council of Argentina (CONICET), Fundación Antorchas, and Secretaría de Ciencia y Tecnología of Universidad Nacional del Sur.

[1] I. W. Hamley, *The Physics of Block Copolymers* (Oxford University Press, Oxford, 1998).
[2] M. W. Matsen, J. Phys.: Condens. Matter **14**, R21 (2002).
[3] M. W. Matsen and M. Schick, Phys. Rev. Lett. **72**, 2660 (1994).
[4] R. R. Li, P. D. Dapkus, M. E. Thompson, W. G. Jeong, C. K. Harrison, P. M. Chaikin, R. A. Register, and D. H. Adamson, Appl. Phys. Lett. **76**, 1689 (2000).
[5] M. Park, P. M. Chaikin, R. A. Register, and D. H. Adamson, Appl. Phys. Lett. **79**, 257 (2001).
[6] K. Asakawa, T. Hiraoka, H. Hieda, M. Sakurai, Y. Kamata, and K. Naito, J. Photopolym. Sci. Technol. **15**, 465 (2002).
[7] J. Y. Cheng, C. A. Ross, E. L. Thomas, H. I. Smith, and G. J. Vansco, Appl. Phys. Lett. **81**, 3657 (2002).
[8] C. K. Harrison, D. H. Adamson, Z. Cheng, J. M. Sebastian, S. Sethuraman, D. A. Huse, R. A. Register, and P. M. Chaikin, Science **290**, 1558 (2000).
[9] C. Harrison, Z. Cheng, S. Sethuraman, D. A. Huse, P. M. Chaikin, D. A. Vega, J. M. Sebastian, R. A. Register, and D. H. Adamson, Phys. Rev. E **66**, 011706 (2002).
[10] C. K. Harrison, Ph.D. thesis, Princeton University, Princeton, 1999 (unpublished).
[11] C. Harrison, D. E. Angelescu, M. Trawick, Z. Cheng, D. A. Huse, P. M. Chaikin, D. A. Vega, J. M. Sebastian, R. A. Register, and D. H. Adamson, Europhys. Lett. **67**, 800 (2004).
[12] M. L. Trawick, M. Megens, C. K. Harrison, D. E. Angelescu, D. A. Vega, P. M. Chaikin, R. A. Register, and D. H. Adamson, Scanning **25**, 2533 (2003).
[13] S. R. Ren and I. W. Hamley, Macromolecules **34**, 116 (2001).
[14] I. W. Hamley, Macromol. Theory Simul. **9**, 363 (2000).
[15] H. Kodama and M. Doi, Macromolecules **29**, 2652 (1996).
[16] S. Komura, J. I. Fukuda, and G. C. Paquette, Phys. Rev. E **53**, R5588 (1996).
[17] H. Zhang, J. Zhang, Y. Yang, and X. Zhou, J. Chem. Phys. **106**, 784 (1997).
[18] Y. Oono and S. Puri, Phys. Rev. Lett. **58**, 836 (1987).
[19] T. Ohta and K. Kawasaki, Macromolecules **23**, 2413 (1990).
[20] T. Ohta and K. Kawasaki, Macromolecules **19**, 2621 (1986).
[21] L. Leibler, Macromolecules **13**, 1602 (1980).
[22] S. Puri and Y. Oono, Phys. Rev. A **38**, 1542 (1988).
[23] J. J. Christensen and A. J. Bray, Phys. Rev. E **58**, 5364 (1998).
[24] Y. Yokojima and Y. Shiwa, Phys. Rev. E **65**, 056308 (2002).
[25] D. A. Vega (unpublished).
[26] J. M. Kosterlitz and D. J. Thouless, J. Phys. C **6**, 1181 (1973).
[27] P. M. Chaikin and T. C. Lubensky, *Principles of Condensed Matter Physics* (Cambridge University Press, Cambridge, U.K., 1995).
[28] D. Moldovan, D. Yamakov, D. Wolf, and S. R. Phillpot, Phys. Rev. Lett. **89**, 206101 (2002).
[29] S. T. Chui, Phys. Rev. B **28**, 178 (1983).
[30] F. L. Somer, Jr., G. S. Canright, T. Kaplan, K. Chen, and M. Mostoller, Phys. Rev. Lett. **79**, 3431 (1997).